Layer-switching mechanisms in Sb2Te3

13 authors, including:

Jiangjing Wang
Xi'an Jiaotong University
13 PUBLICATIONS   **77** CITATIONS

SEE PROFILE

Z. Y. Song
Chinese Academy of Sciences
613 PUBLICATIONS   **5,640** CITATIONS

SEE PROFILE

Lu Lu
Xi'an Jiaotong University
77 PUBLICATIONS   **605** CITATIONS

SEE PROFILE

Hongchu Du
Forschungszentrum Jülich
64 PUBLICATIONS   **762** CITATIONS

SEE PROFILE

Some of the authors of this publication are also working on these related projects:

Carbon Memory View project

Thesis View project

Layer-switching mechanisms in Sb2Te3

Jiang-Jing Wang, Jun Wang, Yazhi Xu, Tianjiao Xin, Zhitang Song, Marc Pohlmann, Marvin Kaminski, Lu Lu, Hongchu Du, Chun-Lin Jia, Riccardo Mazzarello, Matthias Wuttig and Wei Zhang*

Dr. J.-J. Wang
School of Chemistry and Chemical Engineering
Yulin University
Yulin 719000, China

Dr. J.-J. Wang, J. Wang, Y. Xu, Prof. W. Zhang
Center for Advancing Materials Performance from the Nanoscale, State Key Laboratory for Mechanical Behavior of Materials
Xi'an Jiaotong University
Xi'an 710049, China
Email: wzhang0@mail.xjtu.edu.cn

Y. Xu, Prof. R. Mazzarello
Institute for Theoretical Solid-State Physics, JARA-FIT and JARA-HPC, RWTH Aachen University, 52074 Aachen, Germany

T. Xin, Prof. Z. Song
State Key Laboratory of Functional Materials for Informatics, Shanghai Institute of Micro-system and Information Technology
Chinese Academy of Sciences
Shanghai 200050, China.

M. Pohlmann, M. Kaminski, Prof. M. Wuttig
Institute of Physics IA, JARA-FIT and JARA-HPC
RWTH Aachen University
Aachen 52074, Germany

Dr. L. Lu, Prof. C.-L. Jia
The School of Electronic and Information Engineering, State Key Laboratory for Mechanical Behavior of Materials
Xi'an Jiaotong University
Xi'an 710049, China

Dr. H. Du, Prof. C.-L. Jia
Ernst Ruska-Centre for Microscopy and Spectroscopy with Electrons
Forschungszentrum Jülich GmbH,
Jülich 52425, Germany

M. Kaminski, Prof. M. Wuttig

Peter Grünberg Institute (PGI 10)

Forschungszentrum Jülich GmbH

Jülich 52425, Germany

Interfacial phase-change memory (iPCM) based on layer-structured Ge-Sb-Te crystals has been recently proposed, offering an energy-efficient implementation of non-volatile memory cells and supplementing the development of Ge-Sb-Te based phase-change random access memories (PRAMs). Although the working principle of iPCM is still under debate, it is believed that layer-switching plays a role in the switching process between the low-resistance and high-resistance states of iPCM memory cells. However, the role of Ge in forming swapped bilayers—the key elements for layer-switching—is not yet clarified. This work manage to achieve layer-switching in Sb_2Te_3 thin films by manipulating the formation of bilayer defects using magnetron sputtering and post-thermal annealing. By combining scanning transmission electron microscopy (STEM) experiments with density functional theory (DFT) calculations, the essential role of Sb-Te intermixing is elucidated in stabilizing swapped bilayers at a low energy cost. *In situ* STEM experiments provide a real-time and real-space view of dynamical reconfiguration of van der Waals-like gaps in Sb_2Te_3 thin films under electron beam irradiation. The results show that Ge atoms are not necessary for the formation and motion of swapped bilayers, providing atomic insights on the layer-switching mechanism in layer-structured binary and ternary group V- and IV-V-tellurides for memory applications.

Chalcogenide phase-change materials (PCMs) based random access memories (PRAMs) offer a promising route for non-volatile memory chips. PRAMs have entered the global memory market as storage-class memory (SCM) to improve the computing efficiency of electronic devices[1-5]. PRAMs exploit the large electrical contrast between the amorphous and crystalline state of PCMs, e.g. $Ge_2Sb_2Te_5$ (GST), to implement the two logic states '0' and '1'[6-9]. The fast and reversible phase transitions between the two solid states of PCMs correspond to the SET (crystallization) and RESET (amorphization) operations of PRAMs[10-17]. To develop high-performance PRAMs, it is crucial to reduce the power consumption for extensive memory programming. Thermal insulation[18-20], carbon-nanotube integration[21-23] as well as materials engineering[24-26] have been explored for such purpose.

In parallel to improvements on standard PRAMs, energy-efficient memory with different working principle has been proposed and developed, named as interfacial phase-change memory (iPCM)[27-35]. iPCM consists of Chalcogenide superlattices, typically GeTe—Sb_2Te_3. Instead of unconstrained phase transitions between the amorphous and crystalline state, short-range phase transitions through local rearrangements, such as layer-switching between two layered crystalline states of GST, are proposed for iPCM. Although this switching mechanism is still under debate[36-46], layer-switching has been shown to occur in layer-structured GST through swapped bilayers[47-51]. The intermixing of Sb and Te has been proven to be essential for the stabilization of the swapped bilayers[51]. However, it has not yet been clarified whether Ge plays any significant role in the genesis and motion of the swapped bilayers.

In addition to memory applications, layer-structured GST and closely related tellurides, such as $PbBi_4Te_7$, Bi_2Te_3, Sb_2Te_3, are also identified as thermoelectric (TE) materials[52-54] and topological insulators (TI)[55-57]. Structural defects, such as stacking faults, twin boundaries, dislocations as well as antiphase boundaries have been shown to enhance the thermoelectric figure of merit[52, 53] and affect the

topological properties[58, 59] of some of these materials. Therefore, manipulating these defects in these materials is important for thermoelectric and spintronic devices as well.

In this work, we focus on the parent phase Sb_2Te_3, which does not contain Ge and also shows a layered structure in its stable rhombohedral phase. We manipulate the configuration of structural defects in rhombohedral Sb_2Te_3 by synthetic methods and thermal annealing, and obtain Sb_2Te_3 samples with and without swapped bilayers. The structural details, stability and mobility of the bilayers are then studied by scanning transmission electron microcopy (STEM) and density functional theory (DFT) calculations. Our results show that Ge is not crucial for the genesis and motion of the swapped bilayers.

The rhombohedral phase of Sb_2Te_3 can be viewed in a hexagonal lattice system with three Sb_2Te_3 quintuple-layer (QL) atomic blocks and three vacant gaps stacked along the c axis (Figure 1a). The vacant gaps are formed by weakly coupled Te layers, and are commonly referred to as van der Waals (vdW) gaps. Recent work suggested these gaps to be pseudo-vdW gaps, as weak covalent interaction is present in addition to vdW interaction[60, 61]. Hence, we refer these gaps as 'vdW-like gaps' in the following. We grew two sets of Sb_2Te_3 thin films with molecular beam epitaxy (MBE) and magnetron sputtering. MBE is capable of growing high-quality Sb_2Te_3 thin films, while samples produced by sputtering usually contain more disorder. In fact, amorphous chalcogenide thin films are typically formed upon sputtering deposition. In our experiments, the as-grown MBE Sb_2Te_3 samples are in rhombohedral phase, while the sputtered samples are mixtures of amorphous and cubic rocksalt phase[62] upon deposition. The sputtered samples were then annealed at 300 °C for 30 minutes to obtain rhombohedral Sb_2Te_3. The energy dispersive X-ray (EDX) measurements confirm the stoichiometry of both sets of thin films to be Sb_2Te_3 (Figure S1). Further experimental details can be found in the Methods section.

The structural details of the MBE and sputtered samples were investigated at the atomic level by high angle annular dark field (HAADF) imaging on spherical aberration corrected (Cs-corrected) STEM. The intensity peaks (bright dots) in HAADF images correspond to the positions of the atomic columns, and the intensity is approximately proportional to Z^2, where Z represents the averaged atomic number of each column along the view direction[63]. In the MBE samples, regular QL blocks and vdW-like gaps were observed on large scales. No obvious lattice disorder was observed in this set of high-quality thin films (Figure 1b). However, many stacking faults were frequently observed in the sputtered samples (Figure 1c). For instance, some twin-like structures with inversed stacking sequence could be observed, similar to those in GST[51], though the density of such defects is much lower in the Sb_2Te_3 samples. Septuple-layer (SL) nanolamella were more frequently observed, and the size of these nanolamella varies, as indicated by the orange boxes in Figure 1c and Figure S2. SL nanolamella were also identified in Bi_2Te_3[58], and were suggested to tune the carrier concentration and the conduction type. Here, we focus on the bilayer defects, which connect two QL blocks horizontally and lead to the formation of the SL nanolamella, as indicated by the red arrows in Figure 1c. These bilayer defects appear in series and are found frequently in the sputtered samples. They were suggested to be the key element for layer-switching in iPCMs by triggering the reconfiguration of vdW-like gaps[47-49, 51, 64].

To further characterize the chemical details of Sb_2Te_3, HAADF imaging experiments alone are not sufficient, because of the very close atomic number of Sb (51) and Te (52). EDX mapping experiments were thereby carried out in order to unambiguously determine the elemental distribution of Sb and Te. The atomic positions of regular QL blocks are shown in Figure 2a, and the corresponding chemical identifications are shown in Figure 2b-d for Sb, Te and the overlaid map, respectively. Clearly, the stacking of each QL block is –Te-Sb-Te-Sb-Te–, and the QL blocks terminate by two weakly coupled

Te layers, in line with the atomic structure shown in Figure 1a. The structural and chemical details of the bilayer defects are shown in Figure 2 e-h. A clear cross between Sb-rich and Te-rich layers is revealed by EDX mapping, as marked by white and blue circles in Figure 2 f-h. This swapping of Sb-rich and Te-rich layers is very similar to that observed in GST, in spite of the fact that in the current samples Ge is completely absent.

To gain further insights into atomic structure of the swapped bilayers, we perform DFT calculations of perfect and defective rhombohedral Sb_2Te_3. Since the typical length of swapped bilayers is of a few nanometers along the planar direction, large-scale atomic models are necessary to access their structural stability. To this end, orthorhombic supercells of $8.82 \times 1.70 \times 3.08$ nm^3, containing 576 Sb and 864 Te atoms, were constructed. Sequential swapped bilayers were built along the vertical direction. Pairs of bilayers were considered along the planar direction, owing to the periodic boundary conditions employed in the DFT calculations. Each bilayer defect was modelled by using six Sb-Te units, and the Sb-Te intermixing was made along the atomic columns in the view direction.

Atomic relaxations with respect to both atomic positions and cell volume were then performed using the CP2K package (see details in the Methods section). Figures 3a and 3b show visible differences in the structure of the bilayer models with and without Sb-Te intermixing. Upon relaxation, the model with Sb-Te intermixing can clearly sustain the designed bilayers, while the bilayers in the model without intermixing shrink to only two Sb-Te units, corresponding to very sharp switching fronts, see the shaded regions in Figures 3a and 3b. In other words, the size of the bilayers depends on the degree of Sb-Te intermixing and thus could vary, as found in the HAADF images (Figure 1 and Figure S2). The black boxed region in the relaxed model with Sb-Te intermixing (Figure 3a) is taken out for a close check. Figure 3c shows the detailed bonding configuration around the swapped bilayer. HAADF

image simulations were carried out for this part of the model, enabling direct comparisons with

HAADF experimental results. Our simulated HAADF image (Figure 3d) matches well with the

experimental ones (Figure 3e). We also note that the image dots in the bilayers are slightly elongated

in comparison with those in perfect area, as shown in the inset of Figure 3d and 3e. This behavior can

be attributed to the atomic distortions brought by homopolar Sb-Sb and Te-Te bonds in the bilayers.

Due to the heavy computational load, our DFT models contain a much higher defect density than the

real material (Figure 1c). In particular, two bilayers along the horizontal direction were considered to

satisfy the periodic boundary conditions, corresponding to a defect density of 1 bilayer per 4.41 nm

(to be compared with the experimental density of ~1 bilayer per 50 nm). Thus the energy cost per

bilayer, ~1.41 eV/nm (with Sb-Te intermixing, Figure 3a), is overestimated. Nevertheless, such value

is not very significant, and is comparable to the GST case, ~1.67 eV/nm (with Sb-Te intermixing)[51].

For another reference, we also calculated the energy cost per atom of the defective rhombohedral

model with Sb-Te intermixing (Figure 3a) with respect to the perfect rhombohedral one (Figure 1a),

yielding 26 meV/atom. This value is much smaller than the energy difference per atom between the

disordered metastable rocksalt phase and perfect rhombohedral Sb_2Te_3, which is about 75 meV/atom.

In spite of the higher energy, the rocksalt phase turns out to be robust for decades at room

temperatures[62]. We note that the comparison of the energy cost per atom is reasonable, because nearly

all the atoms in the defective rhombohedral models deviate from their original positions due to the

high-density of bilayer defects (Figure 3a). Therefore, we can conclude that the relatively low energy

costs give rise to the formation of swapped bilayers in the sputtered samples. It is important to mention

that the formation of swapped bilayers takes place at 300 °C, at which entropy also plays an effective

role. It is thus expected that the higher energy cost of the bilayers with intermixing is counterbalanced

by their higher entropy. Indeed, the sharp switching fronts are less frequently observed in the sputtered samples at 300 °C.

Furthermore, we performed *in situ* STEM experiments under electron beam irradiation to assess the mobility of the bilayers. We set the switching fronts of two bilayers as a reference, as marked by red stars in Figure 4a. Then we focused the electron beam to the boxed region for 20 minutes. Clearly, the three bilayers move rightward upon irradiation, as indicated by the orange arrows in Figure 4a and 4b. This local structural rearrangement process is in line with the layer-switching process observed in layer-structured GST under electron beam irradiation[47-49] and heating[64, 65]. The chemical details of the rearranged bilayers were further assessed by EDX mapping experiments, which show that the chemical distribution of bilayers remains the same after irradiation (Figure S3). Hence, we prove here that in the absence of Ge, the bilayer motion can proceed in Sb_2Te_3, similarly to that in GST.

In summary, we have managed to manipulate the configuration of lattice defects in rhombohedral Sb_2Te_3 thin films using different synthetic methods. We show that the as-grown epitaxial samples contain no obvious lattice defects, while magnetron sputtering and post-thermal annealing generate extensive stacking faults, as the latter method corresponds to a more complex structural transition path from amorphous and rocksalt Sb_2Te_3 to the rhombohedral phase. The results of HAADF imaging and EDX mapping experiments provide evidences for the –Te-Sb-Te-Sb-Te– stacking sequence in Sb_2Te_3 QL blocks, and elucidate the essential role of Sb-Te intermixing in stabilizing the swapped bilayers. DFT calculations indicate that the relatively low energy cost is the underlying reason for the presence of swapped bilayers and thereby SL nanolamella. Furthermore, we show that the swapped bilayers are mobile under electron beam irradiation. Hence, we can conclude that Ge is not mandatory for the reconfiguration of vdW-like gaps.

Experimental Section

Materials synthesis:

Molecular beam epitaxy (MBE): The Sb_2Te_3 thin films of 150 nm were deposited in the MBE Chamber at a base pressure of about 10^{-11} mbar (10^{-10} mbar during growth). The Si (111) substrate was passivated by Sb to obtain high-quality thin film[66], the deposition rate is 0.2 nm/min. The sample heater was set to 130 °C during deposition. The sources were elemental Sb and Te effusion cells. *Magnetron sputtering*: The ~450 nm Sb_2Te_3 thin film were deposited by magnetron sputtering on a Si (111) substrate. The films were annealed in argon atmosphere (flow rate of 200 sccm) in a regular tube furnace with a 3 cm diameter quartz tube. The annealing temperature was raised to 300 °C with a heating rate of 5 K/min and the samples were kept at 300 °C for 30 min.

Structural characterization and image simulation: The cross-section TEM specimens were prepared by a FEI Helios NanoLab 600i focused ion beam (FIB) system with a Ga ion beam at 30 kV beam energy and polished at 5 kV and 2 kV for cleaning the surface. Atomic-resolution high-angle annular dark field (HAADF) imaging experiments were performed on a JEOL ARM200F and a JEOL ARM300F scanning transmission electron microscope (STEM) with probe aberration correctors, operated at 200 keV and 80 keV, respectively. Energy-dispersive X-ray spectroscopy (EDX) experiments were carried out on the JEOL ARM300F and JEOL JEM2100F microscope at 80 keV and 200 keV, respectively. The HAADF image simulations were carried out using the software packages of Dr. Probe[67]. The accelerating voltage was set to 200 keV, the aperture radius alpha was 25 mrad, and the detection range of HAADF detector was 80~250 mrad.

Ab initio modelling: All density functional theory (DFT) simulations were carried out using the CP2K package[68]. The Kohn-Sham orbitals were expanded in a Gaussian-type basis set of triple-ζ plus polarization quality, whereas the charge density was expanded in the plane-wave basis with an energy cut off of 300 Ry. Both the atomic positions and the simulation cells of all the models presented in this work were fully relaxed by employing the scalar-relativistic Goedecker pseudopotentials[69] and gradient-corrected functionals[70]. Van der Waals corrections were included by using the Grimme's method[71]. The Brillouin zone was sample at Γ point only.

Supporting Information
Supporting Information is available from the Wiley Online Library or from the author.

References

1. M. Wuttig, N. Yamada, *Nat. Mater.* **2007,** *6*, 824.

2. S. Raoux, W. Welnic, D. Ielmini, *Chem. Rev.* **2010,** *110*, 240.

3. H.-S. P. Wong, S. Salahuddin, *Nat. Nanotechnol.* **2015,** *10*, 191.

4. A. V. Kolobov, J. Tominaga, P. Fons, in *Springer Handbook of Electronic and Photonic Materials*, (Eds: S. Kasap, P. Capper), Springer International Publishing AG, **2017**.

5. W. Zhang, R. Mazzarello, M. Wuttig, E. Ma, *Nat. Rev. Mater.* **2019,** *4*, 150.

6. N. Yamada, T. Matsunaga, *J. Appl. Phys.* **2000,** *88*, 7020.

7. I. Friedrich, V. Weidenhof, W. Njoroge, P. Franz, M. Wuttig, *J. Appl. Phys.* **2000,** *87*, 4130.

8. T. Siegrist, P. Jost, H. Volker, M. Woda, P. Merkelbach, C. Schlockermann, M. Wuttig, *Nat. Mater.* **2011, *10***, 202.

9. W. Zhang, A. Thiess, P. Zalden, R. Zeller, P. H. Dederichs, J. Y. Raty, M. Wuttig, S. Blügel, R. Mazzarello, *Nat. Mater.* **2012,** *11*, 952.

10. A. V. Kolobov, P. Fons, A. I. Frenkel, A. L. Ankudinov, J. Tominaga, T. Uruga, *Nat. Mater.* **2004,** *3*, 703.

11. D. Loke, T. H. Lee, W. J. Wang, L. P. Shi, R. Zhao, Y. C. Yeo, T. C. Chong, S. R. Elliott, *Science* **2012, *336***, 1566.

12. J. Orava, A. L. Greer, B. Gholipour, D. W. Hewak, C. E. Smith, *Nat. Mater.* **2012,** *11*, 279.

13. A. Sebastian, M. Le Gallo, D. Krebs, *Nat. Commun.* **2014,** *5*, 4314.

14. R. Jeyasingh, S. W. Fong, J. Lee, Z. Li, K. W. Chang, D. Mantegazza, M. Asheghi, K. E. Goodson, H. S. Wong, *Nano Lett.* **2014,** *14*, 3419.

15. J. Akola, R. O. Jones, *Science* **2017,** *358*, 1386.

16. G. Sosso, G. Miceli, S. Caravati, F. Giberti, J. Behler, M. Bernasconi, *J. Phys. Chem. Lett.* **2013,** *4*, 4241.

17. I. Ronneberger, W. Zhang, H. Eshet, R. Mazzarello, *Adv. Funct. Mater.* **2015,** *25*, 6407.

18. J. Y. Wu, M. Breitwisch, S. Kim, T. H. Hsu, R. Cheek, P. Y. Du, J. Li, E. K. Lai, Y. Zhu, T. Y. Wang, H. Y. Cheng, A. Schrott, E. A. Joseph, R. Dasaka, S. Raoux, M. H. Lee, H. L. Lung, C. Lam, *IEDM Tech. Dig.* **2011,** pp. 3.2.1–3.2.4.

19. C. Ahn, S. W. Fong, Y. Kim, S. Lee, A. Sood, C. M. Neumann, M. Asheghi, K. E. Goodson, E. Pop, H.-S. P. Wong, *Nano Lett.* **2015,** *15*, 6809.

20. S. W. Fong, C. M. Neumann, H.-S. P. Wong, *IEEE Trans. Electron. Dev.* **2017,** *64*, 4374.

21. F. Xiong, A. D. Liao, D. Estrada, E. Pop, *Science* **2011,** *332*, 568.

22. G. W. Burr, M. BrightSky, A. Sebastian, H. Cheng, J. Wu, S. Kim, N. Sosa, N. Papandreou, H. S. Lung, H. Pozidis, E. Eleftheriou, C. Lam, *IEEE J. EM. Sel. Top. C.* **2016,** *6*, 146.

23. E. C. Ahn, H. S. P. Wong, E. Pop, *Nat. Rev. Mater.* **2018,** *3*, 18009.

24. H. Y. Cheng, T. H. Hsu, S. Raoux, J. Y. Wu, P. Y. Du, M. Breitwisch, Y. Zhu, E. K. Lai, E. Joseph, S. Mittal, R. Cheek, A. Schrott, S. C. Lai, H. L. Lung, C. Lam, *IEDM Tech. Dig.* **2011,** pp.3.4.1-3.4.4.

25. M. Zhu, M. Xia, F. Rao, X. Li, L. Wu, X. Ji, S. Lv, Z. Song, S. Feng, H. Sun, S. Zhang, *Nat. Commun.* **2014,** *5*, 4086.

26. F. Rao, K. Ding, Y.-X. Zhou, Y. Zheng, M. Xia, S. Lv, Z. Song, S. Feng, I. Ronneberger, R. Mazzarello, W. Zhang, E. Ma, *Science* **2017,** *358*, 1423.

27. R. E. Simpson, P. Fons, A. V. Kolobov, T. Fukaya, M. Krbal, T. Yagi, J. Tominaga, *Nat. Nanotechnol.* **2011,** *6*, 501.

28. J. Tominaga, A. V. Kolobov, P. Fons, T. Nakano, S. Murakami, *Adv. Mater. Inter.* **2014,** *1*, 1300027.

29. J. Tominaga, *Phys. Status Solidi RRL* **2019,** *13*, 1800539.

30. T. C. Chong, L. P. Shi, R. Zhao, P. K. Tan, J. M. Li, H. K. Lee, X. S. Miao, A. Y. Du, C. H. Tung, *Appl. Phys. Lett.* **2006,** *88*, 122114.

31. W. Zhang, M. Wuttig, *Phys. Status Solidi RRL* **2019**, 13, 1900130.

32. K. V. Mitrofanov, Y. Saito, N. Miyata, P. Fons, A. V. Kolobov, J. Tominaga, *Phys. Status Solidi RRL* **2019**, 1900105. DOI: 10.1002/pssr.201900105.

33. M. Malvestuto, A. Caretta, B. Casarin, F. Cilento, M. Dell'Angela, D. Fausti, R. Calarco, B. J. Kooi, E. Varesi, J. Robertson, F. Parmigiani, *Phys. Rev. B* **2016**, 94, 094310.

34. H. Shirakawa, M. Araidai, K. Shiraishi, *Jpn. J. Appl. Phys.* **2018**, 57 04FE08.

35. Y. Saito, A. V. Kolobov, P. Fons , K. V. Mitrofanov, K. Makino J. Tominaga, J. Robertson, *Appl. Phys. Lett.* **2019**, 114, 132102.

36. X. Yu, J. Robertson, *Sci. Rep.* **2015**, 5, 12612.

37. N. K. Chen, X. B. Li, X. P. Wang, S. Y. Xie, W. Q. Tian, S. Zhang, H. B. Sun, *IEEE Trans. Nanotechnol.* **2017**, 17, 140.

38. X. Yu, J. Robertson, *Sci. Rep.* **2016**, 6, 37325.

39. Y. S. Song, J. Kim, S. H. Jhi, *J. Appl. Phys.* **2017**, 121, 095102.

40. N. Inoue, H. Nakamura, *Faraday Discuss.* **2019**, 213, 303.

41. J. Momand, R. Wang, J. E. Boschker, M. A. Verheijen, R. Calarco, B. J. Kooi, *Nanoscale* **2015,** *7*, 19136.

42. B. J. Kooi, J. Momand, *Phys. Status Solidi RRL* **2019,** *13*, 1800562.

43. M. Boniardi, J. E. Boschker, J. Momand, B. J. Kooi, A. Redaelli, R. Calarco, *Phys. Status Solidi RRL* **2019,** *13*, 1800634.

44. M. Behrens, A. Lotnyk, J. W. Gerlach, I. Hilmi, T. Abel, P. Lorenz, B. Rauschenbach, *Nanoscale* **2018,** *10*, 22946.

45. J. Kalikka, X. Zhou, E. Dilcher, S. Wall, J. Li, R. E. Simpson, *Nat. Commun.* **2016,** *7*, 11983.

46. Xian-Bin Li, Nian-Ke Chen, Xue-Peng Wang, H.-B. Sun, *Adv. Funct. Mater.* **2018,** *28*, 1803380.

47. A. Lotnyk, U. Ross, T. Dankwort, I. Hilmi, L. Kienle, B. Rauschenbach, *Acta Mater.* **2017,** *141*, 92.

48. A. Lotnyk, I. hilmi, U. Ross, B. Rauschenbach, *Nano Res.* **2017,** *11*, 1676.

49. A. V. Kolobov, P. Fons, Y. Saito, J. Tominaga, *ACS Omega* **2017,** *2*, 6223.

50. A. Lotnyk, T. Dankwort, I. Hilmi, L. Kienle, B. Rauschenbach, *Nanoscale*, DOI: 10.1039/C9NR02112D.

51. J.-J. Wang, J. Wang, H. Du, L. Lu, P. C. Schmitz, Johannes Reindl, A. M. Mio, C.-L. Jia, E. Ma, R. Mazzarello, M. Wuttig, W. Zhang, *Chem. Mater.* **2018,** *30*, 4770.

52. B. Xu, T. Feng, Z. Li, L. Zhou, S. T. Pantelides, Y. Wu, *Angew. Chem. Int. Ed.* **2018,** *57*, 10938.

53. X. Fu, Q. Ding, Z. Xu, T. Zhu, Q. Yu, Z. Zhang, *Scripta Mater.* **2017,** *135*, 10.

54. Z. Li, N. Miao, J. Zhou, Z. Sun, Z. Liu, H. Xu, *Nano Energy* **2018,** *43*, 285.

55. Y. L. Chen, J. G. Analytis, J.-H. Chu, Z. K. Liu, S.-K. Mo, X. L. Qi, H. J. Zhang, D. H. Lu, X. Dai, Z. Fang, S. C. Zhang, I. R. Fisher, Z. Hussain, Z.-X. Shen, *Science* **2009,** *325*, 178.

56. M. Z. Hasan, C. L. Kane, *Rev. Mod. Phys.* **2010,** *82*, 3045.

57. B. Sa, J. Zhou, Z. Sun, J. Tominaga, R. Ahuja, *Phys. Rev. Lett.* **2012,** *109*, 096802.

58. Y. Jiang, Y. Wang, J. Sagendorf, D. West, X. Kou, X. Wei, L. He, K. L. Wang, S. Zhang, Z. Zhang, *Nano Lett.* **2013,** *13*, 2851.

59. H. Aramberri, J. I. Cerda, M. C. Munoz, *Nano Lett.* **2015,** *15*, 3840.

60. R. Wang, F. R. L. Lange, S. Cecchi, M. Hanke, M. Wuttig, R. Calarco, *Adv. Funct. Mater.* **2018,** *28*, 1705901.

61. J. Wang, I. Ronneberger, L. Zhou, L. Lu, V. L. Deringer, B. Zhang, L. Tian, H. Du, C. Jia, X. Qian, M. Wuttig, R. Mazzarello, W. Zhang, *Nanoscale* **2018,** *10*, 7363.

62. Y. Zheng, M. Xia, Y. Cheng, F. Rao, K. Ding, W. Liu, Y. Jia, Z. Song, S. Feng, *Nano Res.* **2016,** *9*, 3453.

63. S. J. Pennycook, P. D. Nellist, *Scanning Transmission Electron Microscopy Imaging and Analysis*, Springer-Verlag, New York, USA **2002**.

64. A. Lotnyk, T. Dankwort, I. Hilmi, L. Kienle, B. Rauschenbach, *Scripta Mater.* **2019,** *166*, 154.

65. J. Momand, R. Wang, J. E. Boschker, M. A. Verheijen, R. Calarco, B. J. Kooi, *Nanoscale* **2017,** *9*, 8774.

66. J. E. Boschker, J. Momand, V. Bragaglia, R. Wang, K. Perumal, A. Giussani, B. J. Kooi, H. Riechert, R. Calarco, *Nano Letters* 2014, 14, 3534.

67. J. Barthel, *Ultramicroscopy* **2018,** *193*, 1.

68. J. Hutter, M. Iannuzzi, F. Schiffmann, J. VandeVondele, *WIREs Comput. Mol. Sci.* **2014,** *4*, 15.

69. S. Goedecker, M. Teter, J. Hutter, *Phys. Rev. B* **1996,** *54*, 1703.

70. J. P. Perdew, K. Burke, M. Ernzerhof, *Phys. Rev. Lett.* **1996,** *77*, 3865.

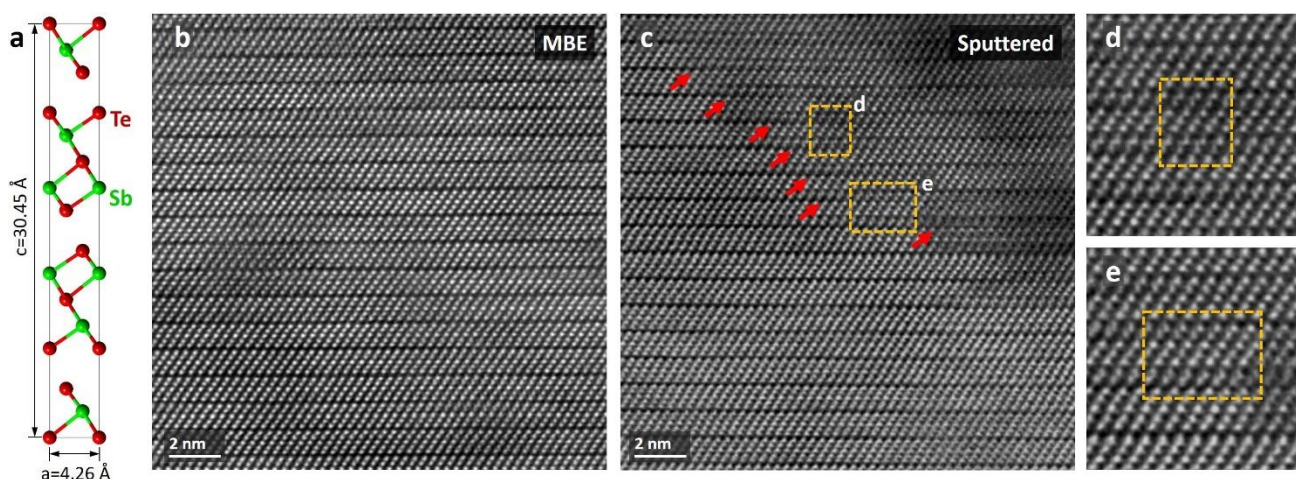71. S. Grimme, *J. Comput. Chem.* **2006,** *27*, 1787.

Figure 1. Structure and thin film of rhombohedral Sb_2Te_3. **a** Crystal structure of rhombohedral Sb_2Te_3. **b-c** Atomic-resolution high-angle annular dark field (HAADF) image of rhombohedral Sb_2Te_3 thin films prepared by **b** molecular beam epitaxy (MBE) and **c** magnetron sputtering and post-thermal annealing. No visible lattice defects are identified in the MBE samples, while extensive stacking faults, in particular, the swapped bilayers (red arrows) and septuple-layer (SL) nanolamella (boxed areas) are observed in the sputtered samples, in addition to the regular quintuple-layer (QL) blocks. **d-e** The zoom-in images of the septuple-layer (SL) nanolamella in **c**.
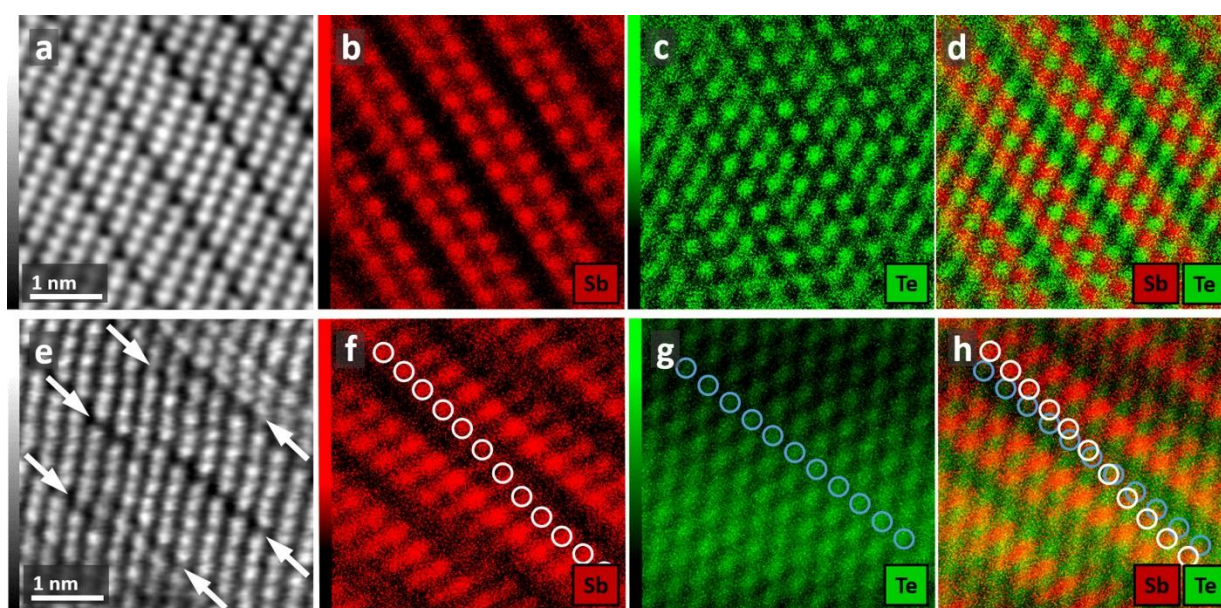
Figure 2. Atomic scale images and chemical maps of sputtered rhombohedral Sb_2Te_3 thin films. **a** The HAADF image, **b-c** the maps of elements Sb and Te, and **d** the overlaid map of the Sb and Te elements. These images and maps confirm the –Te-Sb-Te-Sb-Te– stacking sequence in regular Sb_2Te_3 QL blocks. **e** The HAADF image, **f-g** the maps of elements Sb and Te, and **h** the overlaid map of the Sb and Te elements of the swapped bilayers in Sb_2Te_3. A clear cross between the Sb-rich and Te-rich layers is observed. The overlaid EDX map indicates intermixing of the Sb and Te atoms in the swapped bilayers.
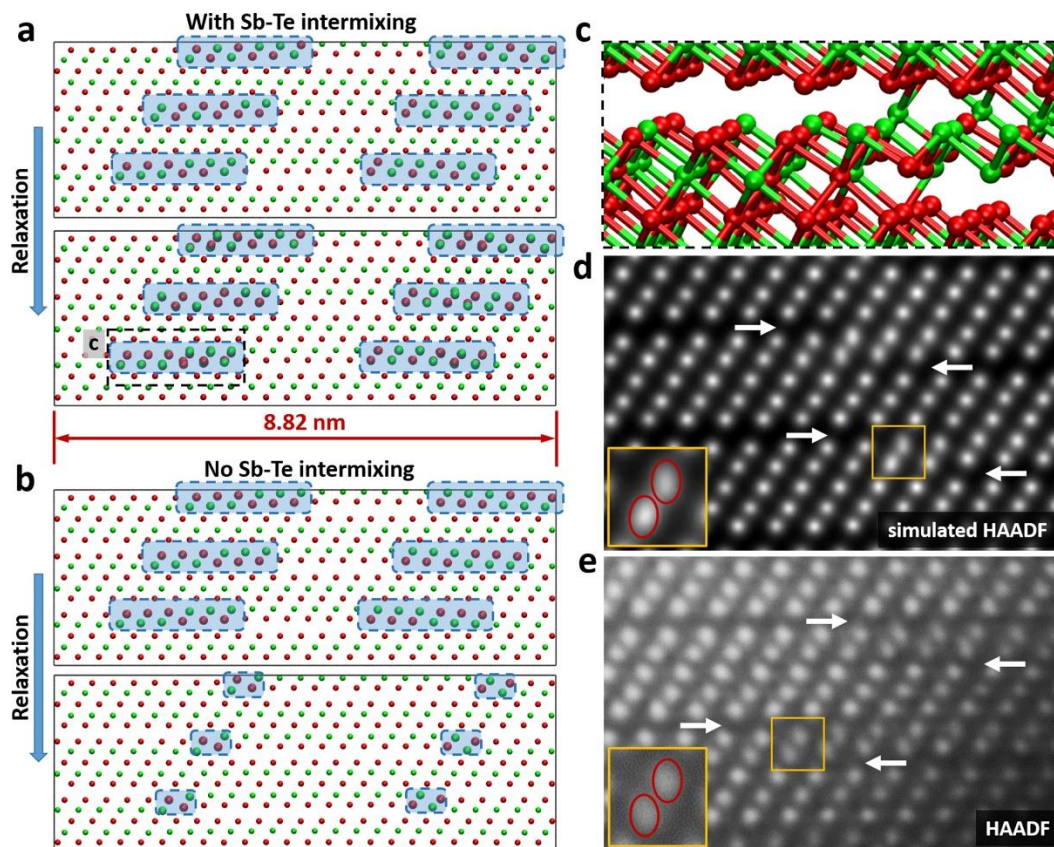

Figure 3. *Ab initio* modelling and HAADF image simulation of the swapped bilayers. **a-b** The as-built and DFT-relaxed atomic models of rhombohedral Sb_2Te_3 with swapped bilayers. Upon atomic relaxation, the Sb-Te intermixed bilayers are robust, while those without Sb-Te intermixing shrink to only two Sb-Te units, corresponding to very sharp switching fronts. In experiments, typical swapped bilayers are found to contain multiple Sb-Te units, revealing the important role of Sb-Te intermixing in forming bilayers. **c** A swapped bilayer in **a** with high magnification, showing the chemical contacts and the details of Sb-Te intermixing along the atomic columns in the view direction. **d** The simulated HAADF image of the atomic model shown in **c**. This simulated image fits well to the experimental one shown in **e**. The insets in **d** and **e** show the elongated dots, due to the atomic distortions brought by Sb-Te intermixing. The white arrows in **d** and **e** point towards the swapped bilayers.
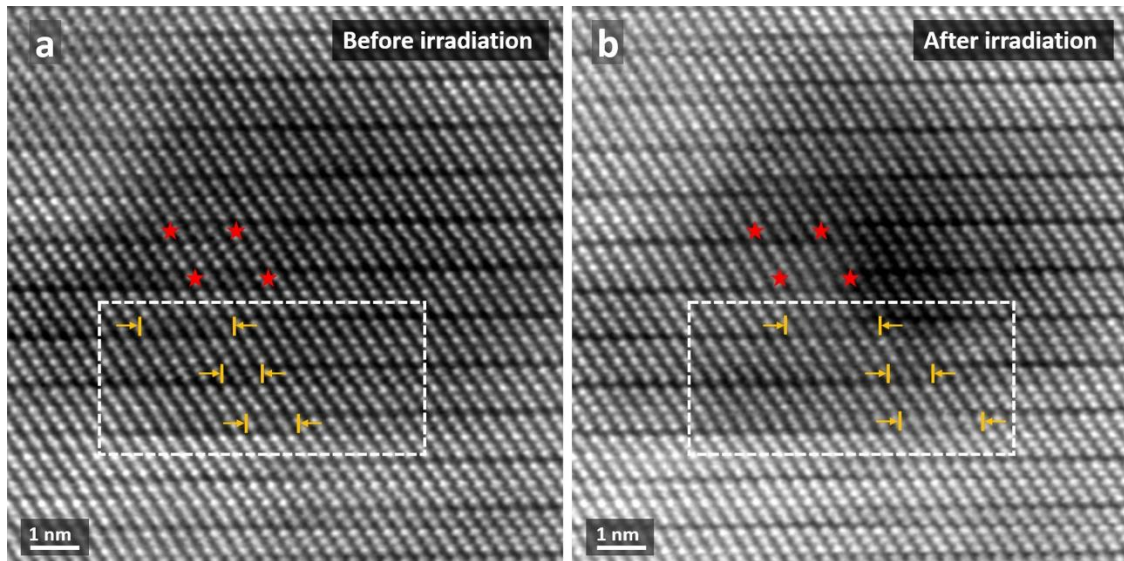
Figure 4. Motion of swapped bilayers in Sb$_2$Te$_3$ thin films under electron beam irradiation. **a-b** The HAADF images of sputtered sample before and after irradiation. The electron beam is focused in the boxed areas. The three bilayers marked by the yellow arrows inside the irradiation region show rightward movement under irradiation over 20 min. Two bilayers above this irradiation area, marked with red stars, are set as the calibration references.